NASA/TM—2013-217850

Solutions of the Taylor-Green Vortex Problem Using High-Resolution Explicit Finite Difference Methods

James R. DeBonis
Glenn Research Center, Cleveland, Ohio

February 2013

NASA STI Program . . . in Profile

Since its founding, NASA has been dedicated to the advancement of aeronautics and space science. The NASA Scientific and Technical Information (STI) program plays a key part in helping NASA maintain this important role.

The NASA STI Program operates under the auspices of the Agency Chief Information Officer. It collects, organizes, provides for archiving, and disseminates NASA's STI. The NASA STI program provides access to the NASA Aeronautics and Space Database and its public interface, the NASA Technical Reports Server, thus providing one of the largest collections of aeronautical and space science STI in the world. Results are published in both non-NASA channels and by NASA in the NASA STI Report Series, which includes the following report types:

- TECHNICAL PUBLICATION. Reports of completed research or a major significant phase of research that present the results of NASA programs and include extensive data or theoretical analysis. Includes compilations of significant scientific and technical data and information deemed to be of continuing reference value. NASA counterpart of peer-reviewed formal professional papers but has less stringent limitations on manuscript length and extent of graphic presentations.

- TECHNICAL MEMORANDUM. Scientific and technical findings that are preliminary or of specialized interest, e.g., quick release reports, working papers, and bibliographies that contain minimal annotation. Does not contain extensive analysis.

- CONTRACTOR REPORT. Scientific and technical findings by NASA-sponsored contractors and grantees.

- CONFERENCE PUBLICATION. Collected papers from scientific and technical conferences, symposia, seminars, or other meetings sponsored or cosponsored by NASA.

- SPECIAL PUBLICATION. Scientific, technical, or historical information from NASA programs, projects, and missions, often concerned with subjects having substantial public interest.

- TECHNICAL TRANSLATION. English-language translations of foreign scientific and technical material pertinent to NASA's mission.

Specialized services also include creating custom thesauri, building customized databases, organizing and publishing research results.

For more information about the NASA STI program, see the following:

- Access the NASA STI program home page at *http://www.sti.nasa.gov*

- E-mail your question to *help@sti.nasa.gov*

- Fax your question to the NASA STI Information Desk at 443–757–5803

- Phone the NASA STI Information Desk at 443–757–5802

- Write to:
  STI Information Desk
  NASA Center for AeroSpace Information
  7115 Standard Drive
  Hanover, MD 21076–1320

NASA/TM—2013-217850

Solutions of the Taylor-Green Vortex Problem Using High-Resolution Explicit Finite Difference Methods

James R. DeBonis
Glenn Research Center, Cleveland, Ohio

Prepared for the
51st Aerospace Sciences Meeting
sponsored by the American Institute of Aeronautics and Astronautics
Grapevine, Texas, January 7–10, 2013

National Aeronautics and
Space Administration

Glenn Research Center
Cleveland, Ohio 44135

February 2013

This work was sponsored by the Fundamental Aeronautics Program
at the NASA Glenn Research Center.

Level of Review: This material has been technically reviewed by technical management.

Available from

NASA Center for Aerospace Information
7115 Standard Drive
Hanover, MD 21076–1320

National Technical Information Service
5301 Shawnee Road
Alexandria, VA 22312

Available electronically at http://www.sti.nasa.gov

Solutions of the Taylor-Green Vortex Problem Using High-Resolution Explicit Finite Difference Methods

James R. DeBonis
National Aeronautics and Space Administration
Glenn Research Center
Cleveland, Ohio 44135

Abstract

A computational fluid dynamics code that solves the compressible Navier-Stokes equations was applied to the Taylor-Green vortex problem to examine the code's ability to accurately simulate the vortex decay and subsequent turbulence. The code, WRLES (Wave Resolving Large-Eddy Simulation), uses explicit central-differencing to compute the spatial derivatives and explicit Low Dispersion Runge-Kutta methods for the temporal discretization. The flow was first studied and characterized using Bogey & Bailley's 13-point dispersion relation preserving (DRP) scheme. The kinetic energy dissipation rate, computed both directly and from the enstrophy field, vorticity contours, and the energy spectra are examined. Results are in excellent agreement with a reference solution obtained using a spectral method and provide insight into computations of turbulent flows. In addition the following studies were performed: a comparison of 4th-, 8th-, 12th- and DRP spatial differencing schemes, the effect of the solution filtering on the results, the effect of large-eddy simulation sub-grid scale models, and the effect of high-order discretization of the viscous terms.

Nomenclature

a_n	spatial finite difference coefficients
b_n	spatial filter coefficients
c, c^*	actual and numerical wave speed
e_t	total energy
p	pressure
q_i	heat flux vector
t	time
t^*	nondimensional time, $t^* = t/(L/V_0)$
u_i	velocity vector
u, v, w	streamwise, transverse and spanwise velocity components
x, y, z	cartesian coordinates
$\mathbf{D}$	spatial finite difference operator
E_k	kinetic energy
$\mathbf{E}(E_k)$	spectral density of kinetic energy
L	reference length
M	Mach number
Re	Reynolds number
S_{ij}	strain rate tensor
S^d_{ij}	deviatoric strain rate tensor, $S^d_{ij} = S_{ij} - S_{kk}\delta_{ij}$
T	temperature
V_0	initial velocity
α_m, β_m	low dispersion Runge-Kutta coefficients
δ_{ij}	Kronecker delta
Δt	time step

Δt^*	nondimensional time step, $\Delta t/(L/V_0)$
ϵ	kinetic energy dissipation rate
ϵ_1	kinetic energy dissipation rate computed from deviatoric strain rate
ϵ_3	kinetic energy dissipation rate computed from pressure dilatation
κ	angular wave number
μ	kinematic viscosity
ν	spectroscopic wave number
ω_i	vorticity vector
Ω	volume
ρ	density
σ	filter damping coefficient
τ_{ij}	stress tensor
ζ	enstrophy

subscripts

0	initial value ($t^* = 0$)

superscripts

$\bar{}$	spatial filtered
$\tilde{}$	Favre filtered
$_{sgs}$	sub grid scale

I. Introduction

The understanding and prediction of turbulent fluid flow continues to be one of the pacing items in the physical sciences. The bulk of turbulent flow predictions are done using Reynolds-Averaged Navier-Stokes (RANS) methods. RANS solves a time-averaged form of the Navier-Stokes equations and the effect of the unsteady turbulent motion on the time-mean flowfield is approximated using a turbulence model. RANS methods perform well for "well-behaved" flows where the models have been calibrated, e.g.. attached boundary layers and mildly separated flows. They fail in more complex flows beyond the bounds of the modeling assumptions, e.g.. large separations, highly anisotropic flows, shock boundary layer interactions, etc. RANS methods rely completely on the model for the prediction of the turbulent flowfield. To reduce or remove the reliance on modeling, methods that resolve some or all of the turbulent motion are gaining usage. Direct numerical simulation (DNS) solves the unsteady Navier-Stokes equations and computes all scales of the turbulent motion and eliminates modeling entirely. Large-eddy simulation (LES) directly computes the large-scale turbulent structures, those that contain most of the turbulent kinetic energy, and uses a model to capture the effects of the smaller unresolved scales, minimizing the model's influence. The success of both DNS and LES rely on the ability of the numerical scheme to accurately compute the unsteady turbulent motion.

The Taylor-Green vortex (TGV) is a canonical problem in fluid dynamics developed to study vortex dynamics, turbulent transition, turbulent decay and the energy dissipation process.[1] The TGV problem contains several key physical processes in turbulence in a simple construct and therefore is an excellent case for the evaluation of turbulent flow simulation methodologies. The problem consists of a cubic volume of fluid that contains a smooth initial distribution of vorticity. Periodic boundary conditions are applied to all boundary surfaces. As time advances the vortices roll-up, stretch and interact, eventually breaking down into turbulence. Because there is no external forcing the small-scale turbulent motion will eventually dissipate all the energy in the fluid and it will come to rest.

In this work we explore the TGV problem using the Wave Resolving Large-Eddy Simulation (WRLES) code[2,3] to gain a better understanding of the interplay between the numerical methods, grid resolution and turbulence, and to validate the code. An initial set of solutions was generated for the First International Workshop on High-Order Methods in Computational Fluid Dynamics, which was held at the American Institute of Aeronautics and Astronautics's Aerospace Sciences Meeting in Nashville Tennessee on January 7-8, 2012. The TGV problem was one of several cases that participants could solve and submit their results for comparison. Additional solutions have since been generated for this paper.

II. Code Description

The code used in this study, WRLES (Wave Resolving Large-Eddy Simulation), is a special purpose large-eddy simulation code that uses high-resolution temporal and spatial discretization schemes to accurately simulate the convection of turbulent structures.[2,3] The code solves the compressible Favre-filtered Navier-Stokes equations on structured meshes using generalized curvilinear coordinates. It is written entirely in Fortran 90 and utilizes both Message Passing Interface (MPI) libraries[4] and OpenMP compiler directives[5] for parallelization.

A. Governing Equations

The basis of large-eddy simulation is the separation of the large and small scale turbulent fluctuations. The large-scale turbulence is computed directly using the Navier-Stokes equations. The small scale turbulence is modeled. Since the large-scales carry the vast majority of the turbulent kinetic energy the technique offers promise for accurate turbulent simulations. Since the small scale turbulence serves to dissipate the large scales and is isotropic, a simple model can be constructed to impose the effect of the small scales on the rest of the flow.

A filtering process is applied to the continuity, momentum, and energy equations. The resulting equations are comprised of resolved and unresolved terms. The resolved terms in the filtered equations directly correspond, in form, to the unfiltered equations. The resulting LES expressions for conservation of mass, momentum, and energy are:

$$\frac{\partial \overline{\rho}}{\partial t} + \frac{\partial}{\partial x_i}\left(\overline{\rho}\tilde{u}_i\right) = 0 \tag{1}$$

$$\frac{\partial}{\partial t}(\overline{\rho}\tilde{u}_i) + \frac{\partial}{\partial x_j}(\overline{\rho}\tilde{u}_i\tilde{u}_j + \overline{p}) = \frac{\partial}{\partial x_j}\left(\overline{\tau}_{ij} + \tau_{ij}^{sgs}\right) \tag{2}$$

$$\frac{\partial}{\partial t}\left(\overline{\rho}\tilde{e}_t\right) + \frac{\partial}{\partial x_i}\left(\overline{\rho}\tilde{u}_i\tilde{e}_t + \tilde{u}_i\overline{p}\right) = \frac{\partial}{\partial x_i}\left[\left(\tilde{u}_j\overline{\tau}_{ij} + \tilde{u}_j\tau_{ij}^{sgs}\right) - \left(\overline{q}_i + q_i^{sgs}\right)\right] \tag{3}$$

The overbar, $\bar{(\,)}$ represents a spatially filtered quantity and the tilde, $\tilde{(\,)}$ represents a Favre-averaged quantity; $\tilde{f} = \overline{(\rho f)}/\bar{\rho}$

The unclosed terms from the LES momentum and energy equations are the sub-grid scale stress, τ_{ij}^{sgs}, and the sub-grid scale heat flux, q^{sgs}. In a traditional LES approach a sub-grid model would be used to compute τ_{ij}^{sgs} and q^{sgs}. Both the standard Smagorinsky model[6] and Lilly's dynamic Smagorinsky model[7] are included in the code. Many practitioners forego sub-grid modeling, relying on the dissipation implicit in the numerical scheme to dissipate the energy at the small-scales. This approach, sometimes called implicit LES (ILES), is used extensively here.

B. Numerical Method

The Favre-filtered Navier-Stokes equations are discretized and solved in strong conservation form using the explicit numerical methods described below.

1. Time Discretization

Time discretization is performed using a family of explicit Runge-Kutta schemes written in a general M-stage 2-N storage formulation.[8]

$$df_m = \alpha_m df_{m-1} + \Delta t \mathbf{D}\left(f_{m-1}\right) \tag{4a}$$

$$f_m = f_{m-1} + \beta_m df_m \tag{4b}$$

for $m = 1 \ldots M$, and where the initial value at the start of the iteration is $f_0 = f^n$ and the final value is $f_M = f^{n+1}$. The coefficient α_1 is typically set to zero for the algorithm to be self-starting. The operator $\mathbf{D}$ is the spatial finite difference operator.

The order of accuracy and dispersion characteristics of the temporal discretization can be varied by changing the number of stages and the coefficients, α_m and β_m. The 4-stage, 3rd-order algorithm of Carpenter and Kennedy[9] was used for all computations in this study.

2. Spatial Discretization

Spatial discretization is performed using central difference methods. The central difference stencil can be written for an arbitrary stencil size

$$\left.\frac{\partial f}{\partial x}\right|_i = \sum_{n=1}^{N} \frac{1}{\Delta x}[a_n(f_{i+n} - f_{i-n})] \tag{5}$$

where the half width of the stencil, the number of points on either side of the central point, is N. The total number of points in the stencil is $2N+1$. The spatial discretization scheme can be varied by simply changing the width of the stencil and the coefficients, a_n. Standard 4th-, 8th- and 12th-order central differences (St04, St08 & St12) and a 13-point dispersion relation preserving (DRP) scheme from Bogey & Bailly[10] (BB13) were used in this study.

Central differencing is used for the spatial discretization because of its non-dissipative properties. Turbulent structures that are well resolved will be accurately convected without being damped. The standard schemes are designed to minimize the truncation error for a given stencil size. The DRP scheme is designed to minimize the dispersion error (phase error) and is formally 4th-order accurate.

3. Filtering

While the lack of dissipation in central differencing is beneficial for the accuracy of turbulent simulations, these schemes are not stable without some form of damping. To ensure a stable solution without adversely affecting the resolving properties of the scheme, solution filtering is used. Solution filtering is a low-pass filter that selectively adds dissipation to damp the high-wavenumber/unresolved structures that lead to instabilities but leaves the low-wavenumber/well-resolved structures untouched. The filter must be properly matched to the differencing scheme, so that the filter removes only those waves that are not properly resolved.

$$\hat{f}_i = f_i + \sigma \sum_{n=-N}^{N} b_n f_{i+n} \tag{6}$$

For the standard central difference schemes, Kennedy and Carpenter's[11] 4th-, 8th- and 12th-order filters (KC04, KC08 & KC12) are used. For the 13-point DRP scheme the matching filter developed by Bogey and Bailly is used (BB13).[10]

4. Properties of the Numerical Scheme

Fourier analysis can be used to evaluate the ability of numerical schemes to resolve wave motion.[12] The technique analyzes the numerical scheme on the one-dimensional convection equation and can provide the scheme's behavior in terms of dissipative and dispersive errors. The effect of the temporal discretization is not considered here.

The analysis shows that central difference schemes have no inherent dissipation, and thus are ideally suited for LES calculations. They do however produce dispersive errors. Figure 1a shows the phase error, written as the ratio of numerical phase speed to actual phase speed, c^*/c, versus normalized angular wave number, $(\kappa\Delta x)$, for the schemes used in this study. For poorly resolved waves, high values of $\kappa\Delta x$, the scheme is unable to accurately resolve the wave.

The damping function of the filter can also be expressed in terms of $\kappa\Delta x$. Figure 1b shows the damping behavior of the KC04, KC08, KC12 and BB13 filters. The damping is minimal until it reaches a "cutoff" wave number, where it rapidly increases, effectively removing all the structures of higher waves numbers. The strength of the filter can be reduced from the default behavior by adjusting a coefficient (ranging from 0 to 1) multiplying the dissipative term.

III. Problem Setup

The TGV problem can be run using a variety of flow conditions and initial conditions. The conditions and post processing used here were specified by the organizers of the AIAA First International Workshop on High-Order Methods in Computational Fluid Dynamics.

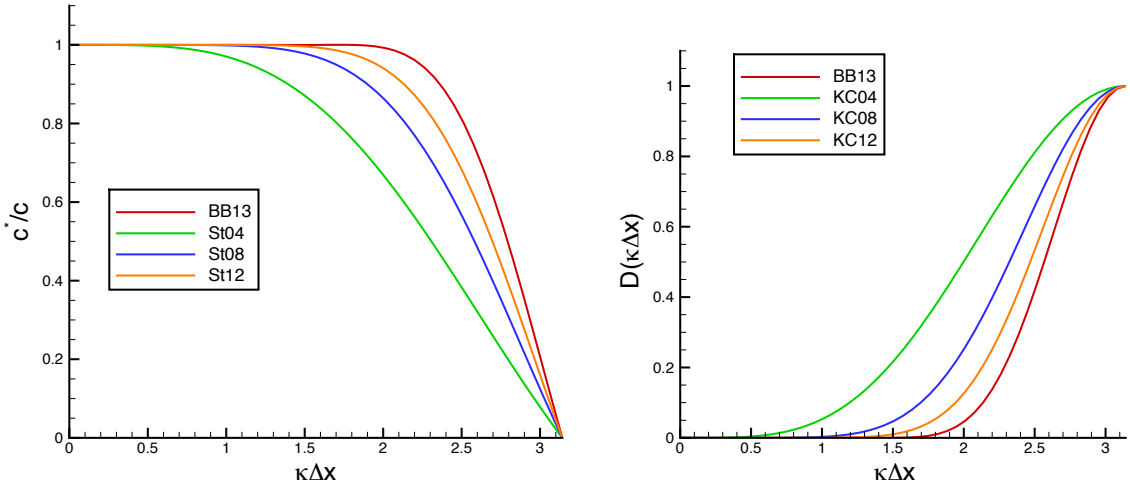

(a) Error in phase speed for the finite difference stencils

(b) Damping functions of the explicit filters

Figure 1: Properties of the numerical scheme

A. Flow Conditions

The domain consists of a cube with sides of length $2\pi L$. Within the domain an initial distribution of velocity and its corresponding vorticity is specified by the following relations.

$$u = V_0 \sin\left(\frac{x}{L}\right)\cos\left(\frac{y}{L}\right)\cos\left(\frac{z}{L}\right) \tag{7}$$

$$v = -V_0 \cos\left(\frac{x}{L}\right)\sin\left(\frac{y}{L}\right)\cos\left(\frac{z}{L}\right) \tag{8}$$

$$w = 0 \tag{9}$$

$$p = p_0 + \frac{\rho_0 V_0^2}{16}\left(\cos\left(\frac{2x}{L}\right) + \cos\left(\frac{2y}{L}\right)\right)\left(\cos\left(\frac{2z}{L}\right) + 2\right) \tag{10}$$

The Reynolds number selected for the workshop was 1600. Because WRLES solves the equations in dimensional form additional flow conditions, given in table 1, were selected to provide an incompressible flow at the given Reynolds number.

Table 1: Flow conditions

Quantity	Value
Reynolds number, Re	1600
Mach Number, M	0.1
Reference length, L	0.005 ft.
Temperature, T	530 R

B. Data Processing

The primary method for evaluating the TGV solutions is examining the rate at which the fluid dissipates the kinetic energy in the domain. The integrated kinetic energy within the domain is computed by

$$E_k = \frac{1}{\rho_0 \Omega}\int_\Omega \rho \frac{u_i u_i}{2} d\Omega \tag{11}$$

The kinetic energy dissipation rate (KEDR) can then be computed by differencing E_k in time.

$$\epsilon(E_k) = -\frac{dE_k}{dt} \tag{12}$$

This KEDR, ϵ, is written as a function of E_k to emphasize that it is computed directly from the kinetic energy in the domain.

A second "theoretical" kinetic energy dissipation rate can be computed from the integrated enstrophy, ζ, within the domain

$$\zeta = \frac{1}{\rho_0 \Omega} \int_\Omega \rho \frac{\omega_i \omega_i}{2} d\Omega \tag{13}$$

It can be shown that for incompressible flow, the enstrophy is directly related to the kinetic energy dissipation rate through a constant.

$$\epsilon(\zeta) = 2\frac{\mu}{\rho_0}\zeta \tag{14}$$

The difference between the directly computed KEDR, $\epsilon(E_k)$, and the enstrophy based KEDR, $\epsilon(\zeta)$, will be examined.

Two additional quantities were computed to test the incompressible assumption. For a compressible flow where the bulk viscosity can be taken to be zero, the "theoretical" dissipation rate is the sum of two quantities; the contribution to the KEDR, obtained from the deviatoric strain rate tensor

$$\epsilon_1 = 2\frac{\mu}{\rho_0 \Omega} \int_\Omega S_{ij}^d S_{ij}^d d\Omega \tag{15}$$

and the contribution to the KEDR, obtained from the pressure dilatation term.

$$\epsilon_3 = -\frac{1}{\rho_0 \Omega} \int_\Omega p \frac{\partial u_i}{\partial x_j} d\Omega \tag{16}$$

For low Mach number flows ϵ_3 should be negligible and the "theoretical" dissipation rate can be approximated using the enstrophy based KEDR (equations 13 & 14).

C. Grids

The grids were generated using a Fortran code that also computed the initial solution at $t^* = 0$. The grids are equally spaced cartesian grids of 64^3, 128^3, 256^3, and 512^3 points. In order to maintain the high-order of accuracy at the boundaries of the domain, 11 additional planes are added beyond the $x = +\pi L$, $y = +\pi L$ and $z = +\pi L$ boundaries and periodic conditions are enforced over a range of 6 points adjacent to the boundaries. This insures that all points within the domain are computed using the full finite difference stencil and filter stencil, and that the resolution of the scheme is maintained.

IV. Results

For the baseline and numerical scheme investigations, grid resolution studies were performed using grids of 64^3, 128^3, 256^3, and 512^3 points. For each differencing scheme and grid, the coefficient that multiplies the effect of the filter was halved until a minimum value was found that provided a stable solution with minimal dissipation. It was found that this minimum filter coefficient was the same for all grid resolutions for a given scheme. The nondimensional time step used for the 64^3 case was $\Delta t^* = 3.385 \cdot 10^{-3}$. The time step was halved for each doubling of the grid dimensions.

The 64^3 and 128^3 cases were run on a single processor desktop workstation with six cores. The larger cases were run on the NASA Pleaides high performance computing system using 8, 8-core processors for the 256^3 cases and 46, 8-core processors for the 512^3 cases. Approximate wall clock time for the runs is given in table 2. The WRLES code was originally written for the 13-point DRP scheme. The full 13-point stencil is always solved and there is no reduction in work for the low-order schemes. The other schemes are implemented by changing the differencing stencil coefficients and zeroes are used where necessary for the low-order schemes. For this reason there is no CPU time difference between schemes.

Table 2: Computing resources

grid size	time step (Δt^*)	machine	cores	wallclock time (hrs.)
64^3	$3.385{\cdot}10^{-3}$	desktop	6	0.5
128^3	$1.693{\cdot}10^{-3}$	desktop	6	9
256^3	$8.463{\cdot}10^{-4}$	Pleiades	64	40
512^3	$4.231{\cdot}10^{-4}$	Pleaides	368	130

Numerous solutions were run to support the following studies

- Baseline study using the 13-point Bogey and Bailley DRP scheme (BB13)
- Comparison of numerical schemes: standard 4th (ST04), 8th (ST08) and 12th (ST12) order central differencing and 13pt. DRP scheme (BB13)
- Examination of the energy spectra
- Effect of the filter
- Effect of sub-grid stress model
- Effect of the order of accuracy of the viscous term derivatives

A. Baseline

A baseline set of simulations was performed using the BB13 scheme. Four grid levels were run and a filter coefficient of 0.05 was used for all the cases. Iso-contours of the z-component of vorticity (figure 2) illustrate the evolution of the flow as described by Brachet in reference 13. At the earliest times the flow behaves inviscidly as the vortices begin to evolve and roll-up. Near $t^* = 7$ the smooth vortical structures begin to undergo changes in their structure and around $t^* = 9$ the coherent structures breakdown. Beyond this breakdown, the flow is fully turbulent and the structures slowly decay until the flow comes to rest.

The change in the kinetic energy over time is shown for all four grid levels in figure 3. Little difference is seen between the grid levels in this plot; although a close-up of $10 < t^* < 20$ indicates that the coarser the grid, the less energy it contains as time evolves.

Figure 4 shows the turbulent decay process. The directly computed KEDR, $\epsilon(E_k)$, is given in figure 4a. Reasonable agreement with the reference solution[14] is show for all grid levels. The largest discrepancies are at the peak dissipation rates, $7 < t^* < 12$. At $t^* = 9$, where the dissipation rate peaks, the 128^3, 256^3, and 512^3 grids are all within two percent of the reference solution (the 64^3 grid has an error of 9.8 percent).

The KEDR computed using the enstrophy integral, $\epsilon(\zeta)$, is given in figure 4b. In theory the enstrophy based KEDR should be equivalent to the directly computed KEDR, but it is clear that there is a large discrepancy in the peak dissipation rate for the lower grid levels (46 percent for the 64^3 case) that improves with grid resolution. The 256^3 (within 2.5 percent) and 512^3 (within one percent) grids are in excellent agreement with the reference solution.

The contributions to the KEDR based on compressible flow assumptions are shown in figures 4c and 4d. The primary contribution to the KEDR is through ϵ_1 and the data shows that it is identical to the incompressible $\epsilon(\zeta)$ predictions. The pressure - dilatation contribution, ϵ_3, is two-orders of magnitude smaller than ϵ_1 and can be neglected. The ϵ_3 curve for the 256^3 case differs from the other cases beyond $t^* > 8$. This behavior is unexplained and does not affect the results. These results confirm the incompressible flow assumption, and it will be used for the remaining analysis and discussion.

Contours of the vorticity norm on the constant x-plane, $x = -\pi L$, at time $t^* = 8$ are shown in figure 5. On the 64^3 grid, the vorticity is smeared over a large area, the structure is jagged and not well defined, and the peak levels are low relative to the higher resolution grids. As resolution is increased, the structure becomes less smeared, smoother and more defined, and the peak vorticity level increases. There are minimal differences between the 256^3 and the 512^3 solution and those plots closely resemble the reference solution shown by van Rees.[14] The increased resolution of the vortical structures with grid resolution seen here,

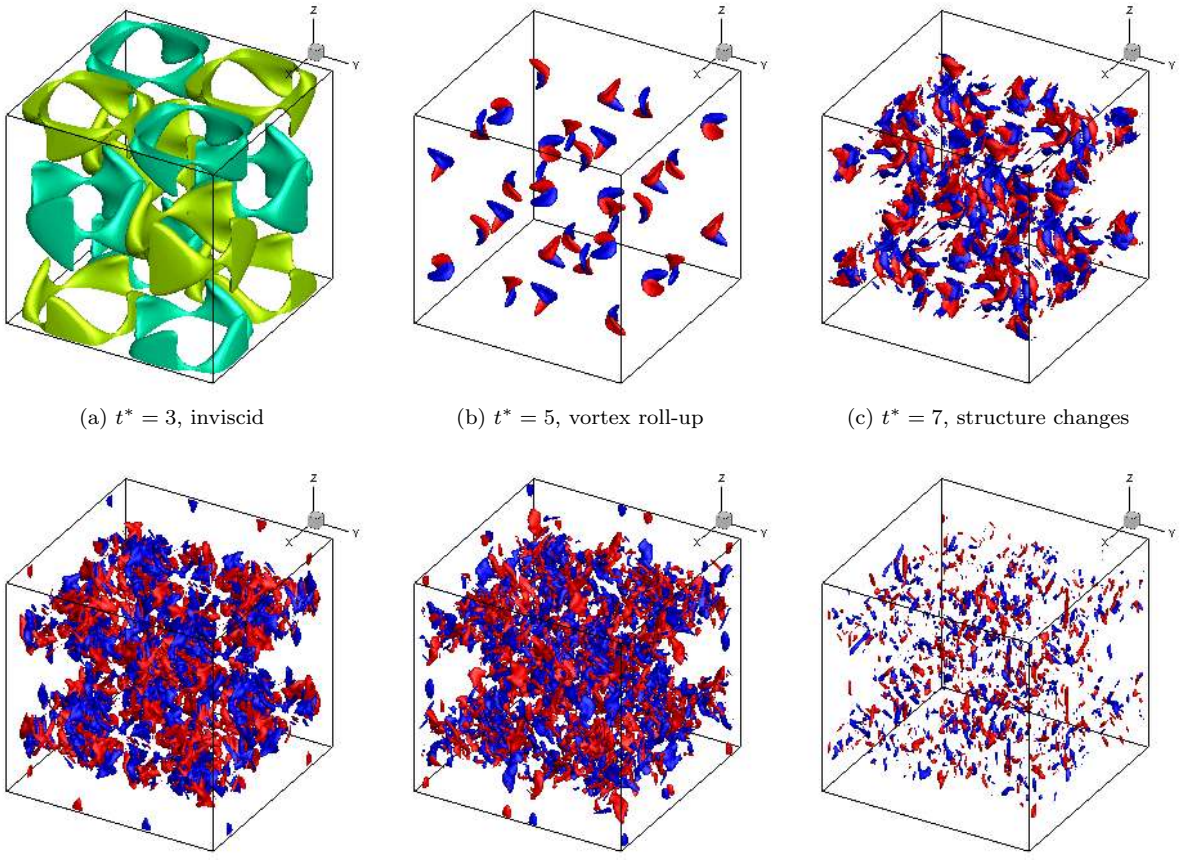

(a) $t^* = 3$, inviscid (b) $t^* = 5$, vortex roll-up (c) $t^* = 7$, structure changes

(d) $t^* = 9$, coherent breakdown (e) $t^* = 11$, fully turbulent (f) $t^* > 11$, turbulent decay

Figure 2: Iso-surfaces of z-vorticity from the BB13 scheme on the 128^3 grid

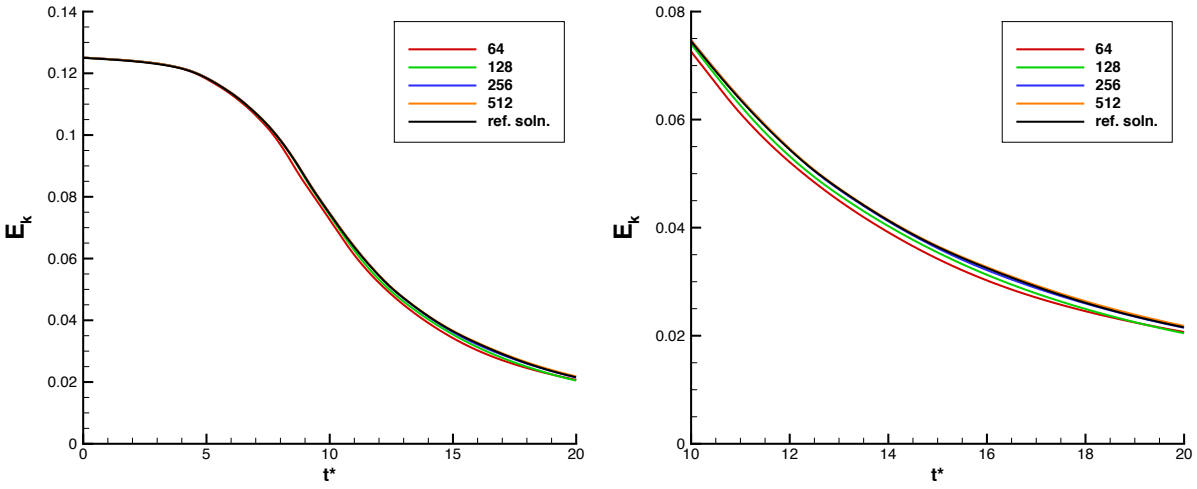

(a) complete simulation, $0 < t^* < 20$ (b) close up of $10 < t^* < 20$

Figure 3: Evolution of kinetic energy

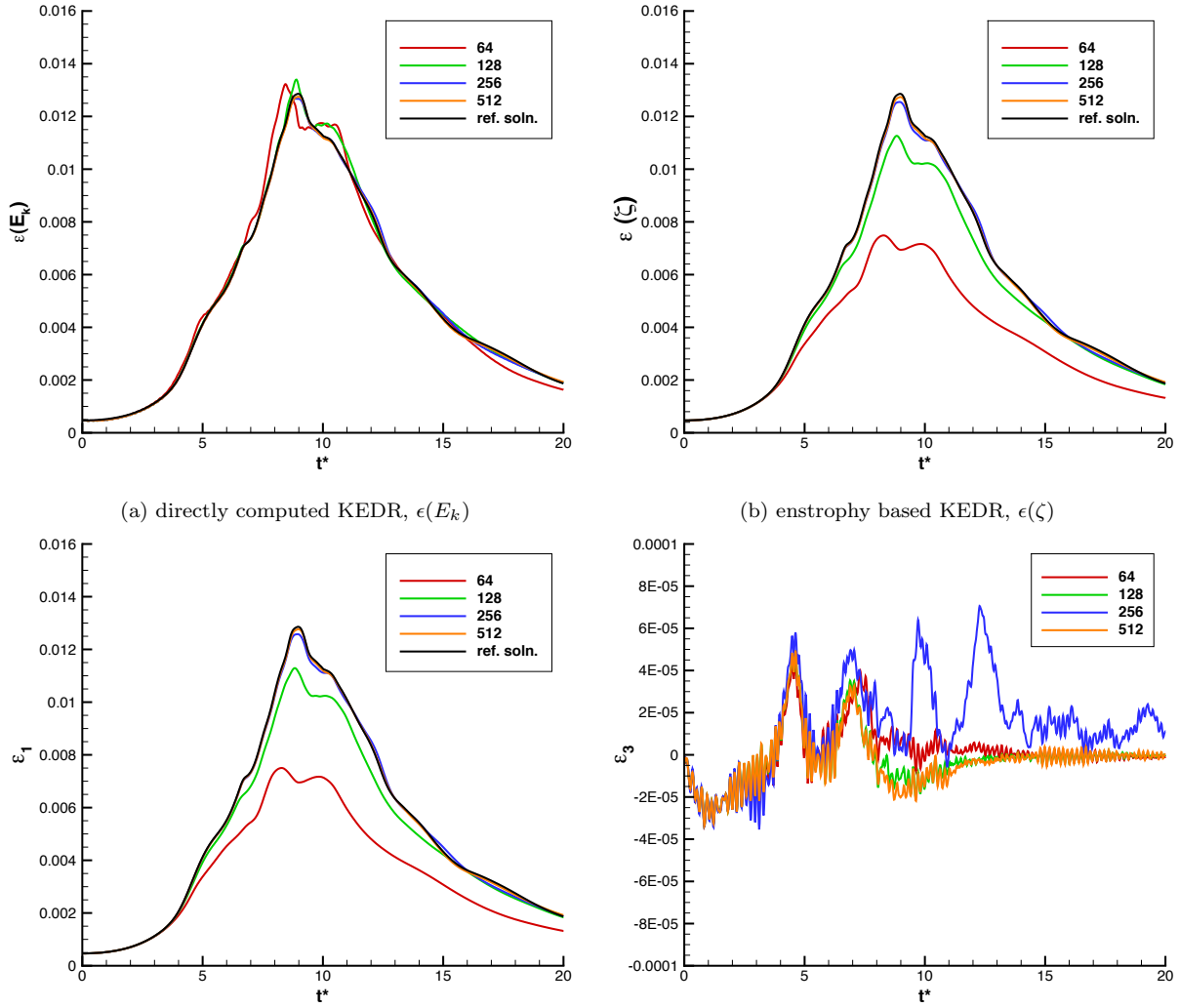

(a) directly computed KEDR, $\epsilon(E_k)$

(b) enstrophy based KEDR, $\epsilon(\zeta)$

(c) deviatoric strain tensor based KEDR, ϵ_1

(d) pressure dilatation based KEDR, ϵ_3

Figure 4: Kinetic energy dissipation rate; comparison of grid resolutions using the BB13 scheme directly corresponds to the improved prediction of KEDR computed from the enstrophy (equation 13) shown in figure 4b; enstrophy is simply the square of the vorticity magnitude.

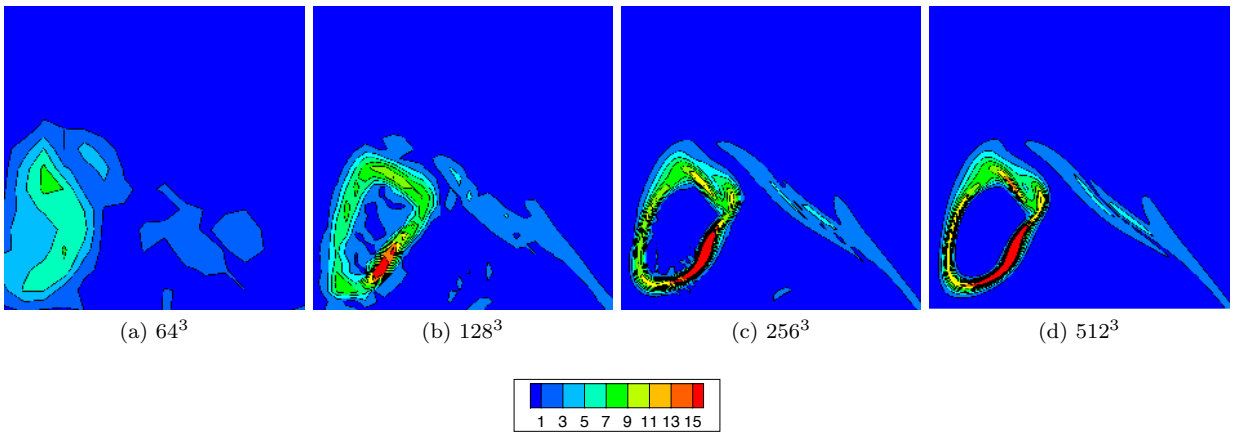

(a) 64^3 (b) 128^3 (c) 256^3 (d) 512^3

Figure 5: Contours of the vorticity norm $|\omega|\frac{L}{V_0}$, at $t^* = 8$ on the plane $x = -\pi L$, in the region $y = 0$ to $\frac{\pi L}{2}$ and $z = \frac{\pi L}{2}$ to πL; comparison of grid resolutions using the BB13 scheme

The discrepancy between $\epsilon(E_k)$ and $\epsilon(\zeta)$ provides valuable insight into turbulent simulations. Despite the huge variation in resolution (a factor of 512 in the number of grid points between the 64^3 and 512^3 simulations) the kinetic energy in the domain (figure 3) and the directly computed KEDR ($\epsilon(E_k)$) (figure 4a) are well predicted at all grid levels. However, at lower grid resolutions, the KEDR computed from the enstrophy ($\epsilon(\zeta)$) is significantly lower than the directly computed KEDR. In other words the dissipation due to the vorticity (i.e. turbulence) does not account for all the dissipation present in the simulation. An additional mechanism is present and it plays a significant role at low resolutions. This mechanism is numerical dissipation.

For the WRLES code the numerical dissipation is generated solely by the spatial filter. As the grid is refined the resolution of the vortical structures increases, increasing $\epsilon(\zeta)$ and the effect of the filter decreases, reducing numerical dissipation. The fact that $\epsilon(E_k)$ is well predicted at all grid levels indicates: 1) the two sources of dissipation in the calculation are in proper proportion to each other and 2) the filter correctly mimics the physical dissipation process of the unresolved scales. This validates the use of these numerical methods for implicit large-eddy simulations. The addition of an explicit sub-grid model will be examined in a later section.

B. Comparison of Schemes

A comparison of the four spatial differencing schemes on all grid levels is shown in figure 6. The directly computed and theoretical KEDR are shown. The results are consistent with the baseline study (figure 4). The directly computed kinetic energy dissipation rate agrees reasonably well for all grid levels and schemes, with the exception of the 4th-order scheme on the 64^3 grid, where the combination of lower-order scheme and coarse grid can not resolve the flow adequately and the resulting KEDR curve exhibits a different character from the others. The enstrophy based KEDR is under-predicted for all schemes until the 256^3 grid is reached. The lower order schemes all approach the correct $\epsilon(\zeta)$ levels with grid refinement, but the 4th-order scheme requires additional refinement beyond 256^3. The ST12 and BB13 schemes, both utilize 13 point stencils and their predictions are very similar with some differences occurring near the peak dissipation and beyond.

C. Examination of Spectra

Kinetic energy spectra were computed to show the evolution and decay of the turbulent structures. Spectra were computed along each grid line and averaged. A saw-tooth shaped odd–even grid point oscillation in the spectra was seen for all cases. Brachet[13] also reported this behavior and averaged the spectra over twice the band width ($2\pi L\Delta\nu = 2$) to remove the oscillation. This averaging was used here as well.

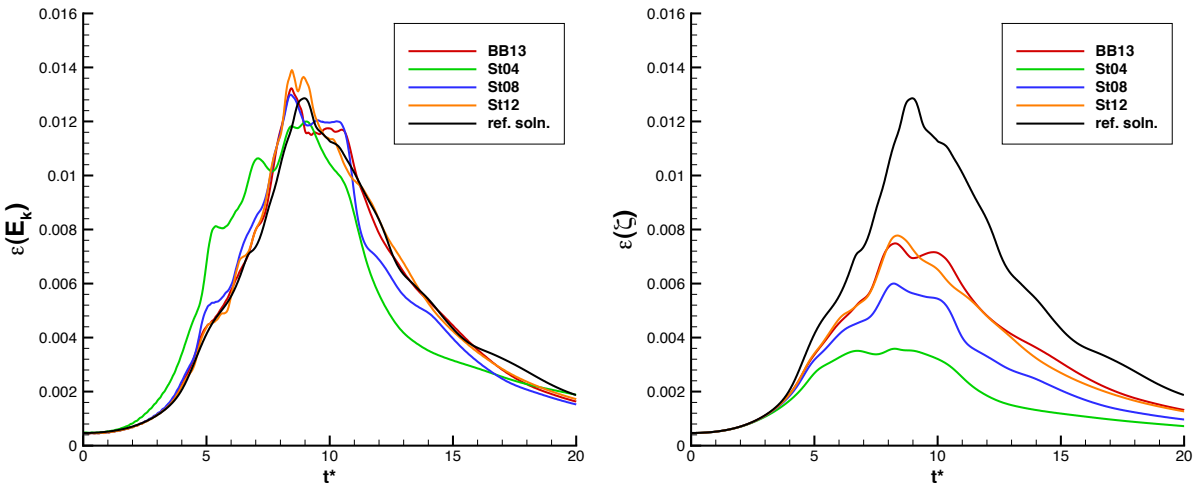

(a) 64^3 grid

(b) 64^3 grid

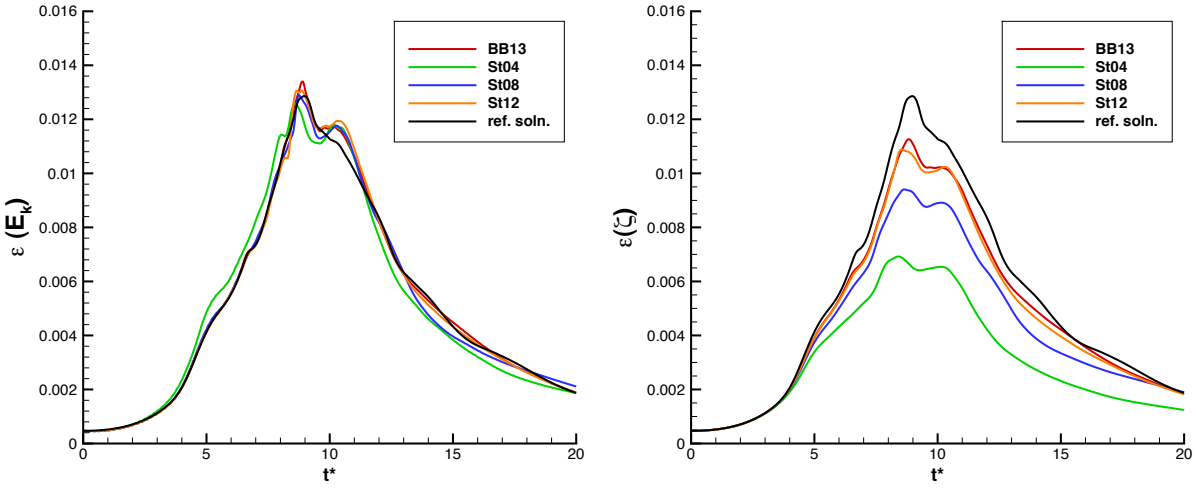

(c) 128^3 grid

(d) 128^3 grid

Figure 6: Kinetic energy dissipation rate; comparison of finite differencing schemes. Left column, directly computed KEDR, $\epsilon(E_k)$, right column, enstrophy based KEDR, $\epsilon(\zeta)$

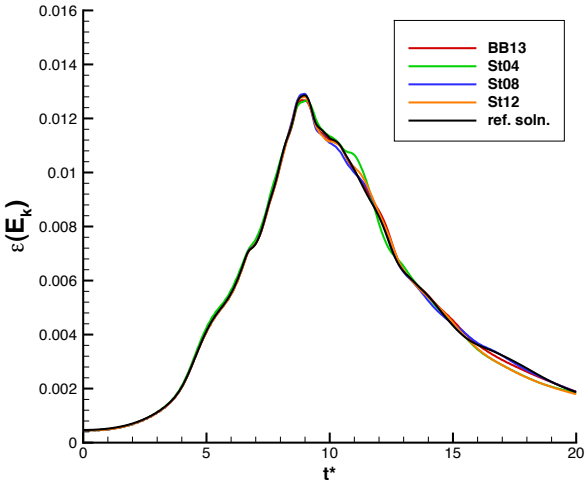

(e) 256^3 grid

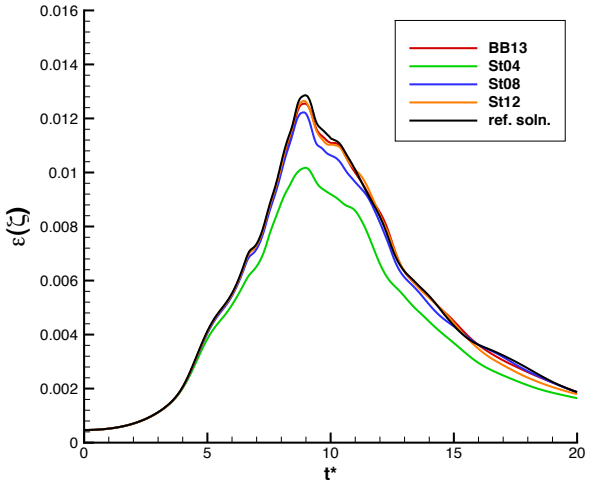

(f) 256^3 grid

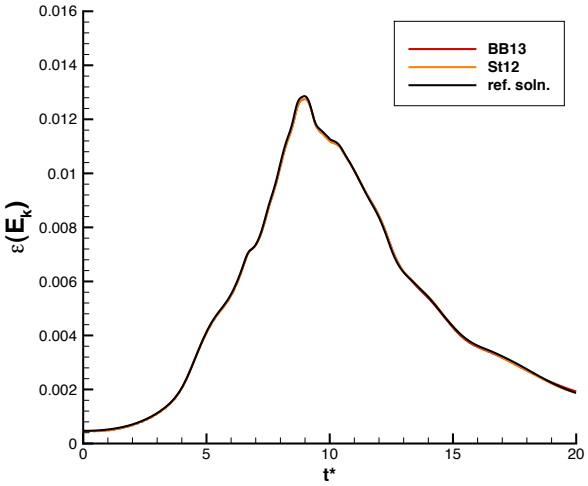

(g) 512^3 grid

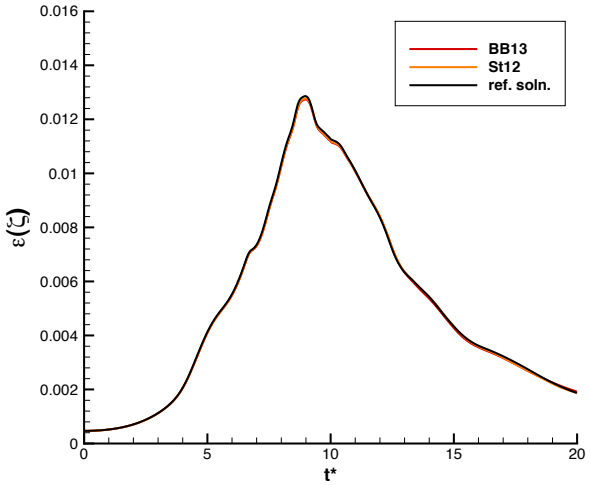

(h) 512^3 grid

Figure 6: (continued) Kinetic energy dissipation rate; comparison of finite differencing schemes. Left column, directly computed KEDR, $\epsilon(E_k)$, right column, enstrophy based KEDR, $\epsilon(\zeta)$

The progression of the energy spectra with time on the 512^3 grid is shown in figure 7. At $t^* = 2$ all the energy is confined to small wave numbers. As time progresses, the energy begins to cascade down to smaller and smaller scales. The energy in the smallest scales peaks around $t^* = 10$. This corresponds to the maximum energy dissipation rate. Beyond this time, the energy decays for all wave numbers.

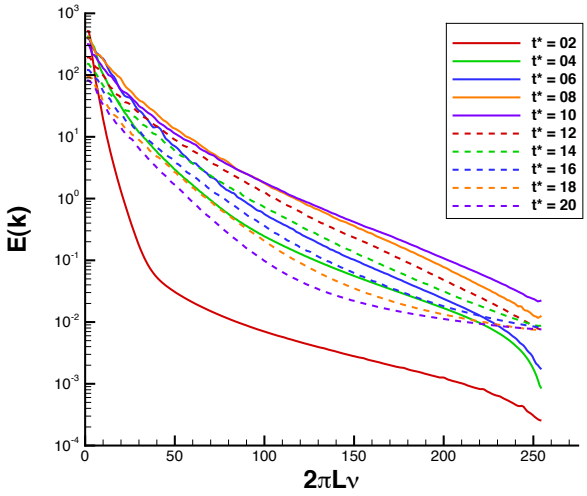

Figure 7: Evolution of the energy spectra for the BB13 scheme on the 512^3 grid

The spectra for $t^* = 12$ for both the BB13 and ST12 schemes on all grid levels are shown in figure 8. For the lower grid resolutions one can see that the energy near the end of the spectra "tails off," falling below the higher resolution curves. This reduction in energy is the result of the filter dissipating the energy at the highest wave numbers in the solution, where the differencing scheme is producing dispersion errors. Refining the grid moves this effect to higher and higher wave numbers. The difference between the ST12 and BB13 schemes is also illustrated by the spectra. The DRP schemes trade formal order of accuracy for improved resolution of waves. Careful comparison of the close-up plot shows that for a given grid resolution the energy in the ST12 solution begins to fall away from the higher resolution curves sooner than the BB13 solution. However the difference is slight.

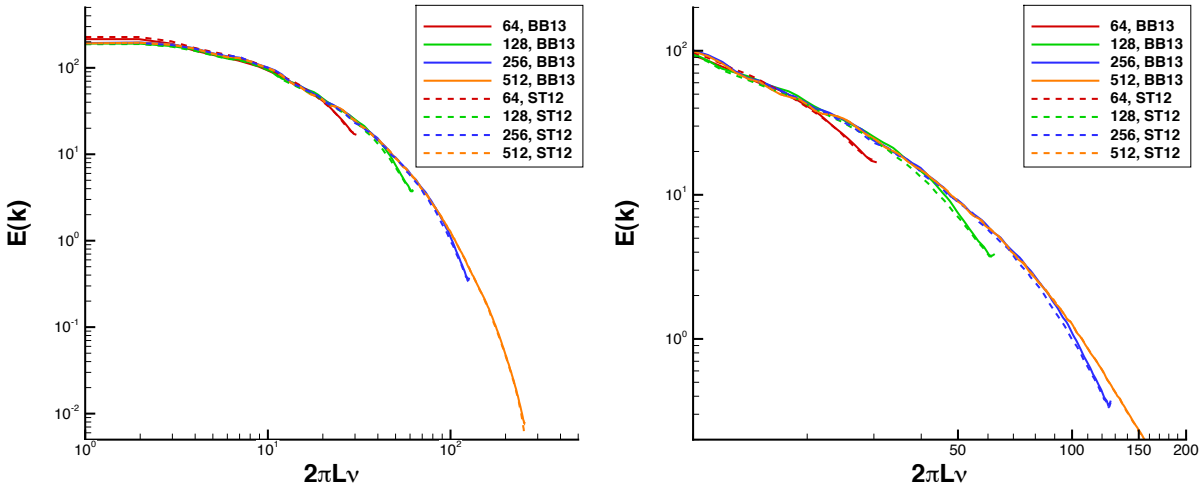

(a) energy spectra at $t^* = 12$

(b) close-up of energy spectra at $t^* = 12$

Figure 8: Energy spectra at $t^* = 12$ for the BB13 and ST12 schemes

D. Effect of the Filter

Artificial/numerical dissipation is present in some form in all CFD codes. This dissipation is necessary to obtain stable solutions, but too much dissipation can have an adverse effect on the results. This is especially true for DNS and LES analyses where the numerical dissipation can easily damp the turbulent structures that are critical for an accurate solution. For the WRLES code, artificial dissipation is incorporated through the filter. There are two key parameters that control the filtering process: 1) the shape of the filter response (unique to each filtering scheme) and 2) the damping coefficient, σ. For this study the BB13 scheme was used to solve the TGV problem on a 128^3 grid. Three filtering schemes were examined: 1) the baseline case using the matching BB13 filter and the minimum stable damping coefficient of 0.05, 2) the BB13 filter and the maximum damping coefficient of 1.0 and 3) the 6th-order Kennedy & Carpenter filter, KC06, and a damping coefficient of 0.05.

Figure 9 shows the evolution of the kinetic energy for the 3 filtering schemes. Increasing the damping coefficient maintains the shape of the filter response and simply increases the amount of damping across all wave numbers. This is reflected in the fact that the shape of the kinetic energy curve is maintained, but the amount of energy is reduced. This is also illustrated by examining the kinetic energy spectra at $t^* = 12$ (figure 10). The shape of the two BB13 filter curves is very similar, but the $\sigma = 1.0$ curve contains less energy across the entire spectra. Changing the filter to KC06, reduces the cutoff wave number; this will remove larger turbulent structures. By removing larger structures the solution initially contains less energy ($5 < t^* < 10$). But because the large scale turbulent structures are responsible for dissipating energy the turbulent dissipation is lessened at later times and the kinetic energy is greater than the baseline solution beyond $t^* = 15$. The spectra for the KC06 curve (figure 10) shows similar energy content at the low wavenumbers, but the energy contained at the higher wave numbers is reduced.

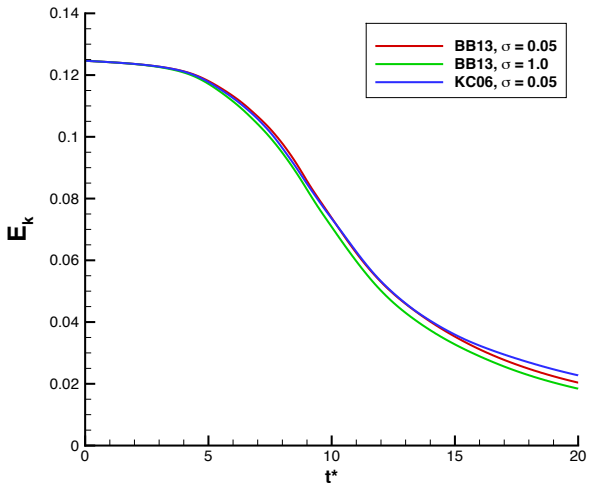

Figure 9: Evolution of kinetic energy, BB13 scheme on the 128^3 grid; effect of filter order

The kinetic energy dissipation rates are shown in figure 11. These plots confirm the above observations. For both modified dissipation cases, the additional damping causes an increase in KEDR for the first half of the simulation. Near the peak dissipation, the KC06 case shows significantly less $\epsilon(E_k)$ because there are less large scale structures. The added dissipation across all wavenumbers for the maximum coefficient case also shows a reduction in $\epsilon(E_k)$, but not to the same extent. As expected the enstrophy based KEDR indicates that both cases significantly increase the amount of numerical dissipation in the simulation; the KC06 case being the most dissipative.

In section C the pronounced reduction in the magnitude of the spectra at the highest resolved wave numbers was attributed to the filter. This effect is examined more closely here. The error in the spectra on a given grid was obtained by comparing that spectra to the spectra on the highest resolution grid (512^3), $|\mathbf{E}(k)_{512} - \mathbf{E}(k)_n|$. This error, for the BB13 scheme on the 256^3 grid, is shown in figure 12. The error is plotted against the normalized angular wave number. The damping function of the filter is plotted for comparison.

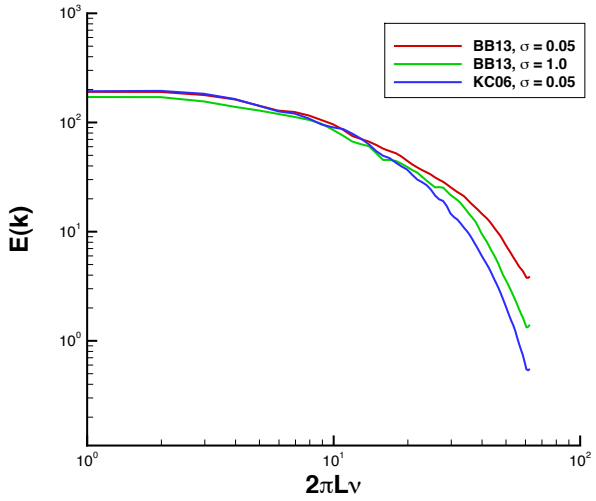

Figure 10: Energy spectra, BB13, 128^3 grid; effect of filter parameters

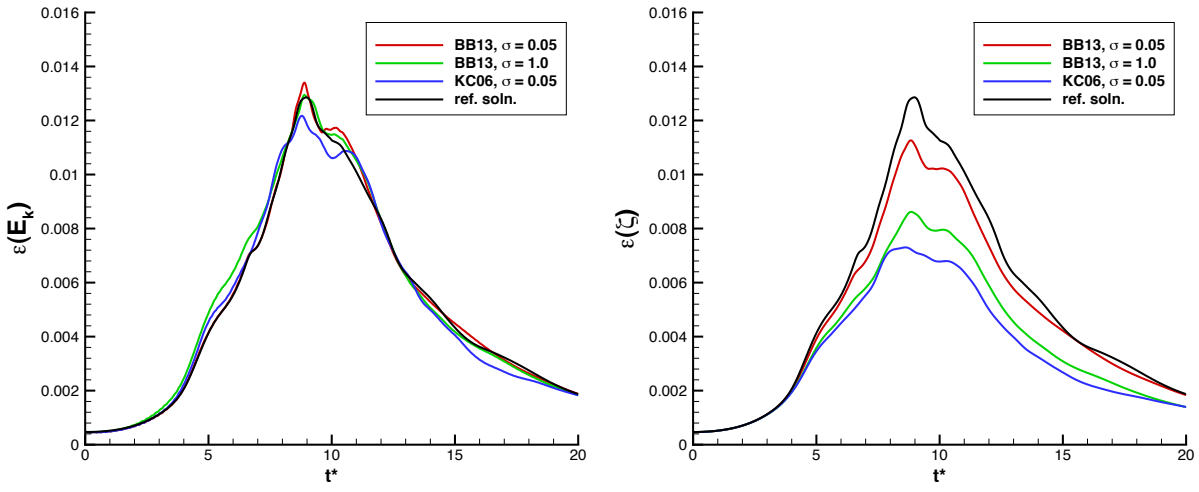

(a) directly computed KEDR, $\epsilon(E_k)$

(b) enstrophy based KEDR, $\epsilon(\zeta)$

Figure 11: Evolution of kinetic energy and kinetic energy dissipation rate; effect of filter parameters

For $t^* \leq 4$ (figure 12a) there is no discernible trend; perhaps because the flow is still transitioning and the spectra are not fully developed. At later times (figure 12b) a clear trend is seen: 1) at low wave numbers the error is low, 2) at approximately $k\Delta x = 2$ the error begins to rise steadily, and 3) the error mimics the shape of the filter's damping function. Clearly, the filter is removing the energy beyond the nominal cut-off wave number of $k\Delta x \approx 2$ while leaving the well resolved wave numbers untouched. The $t^* = 20$ curve does not follow these trends and the reason is unknown. The observations made here are also valid for the other grid resolutions.

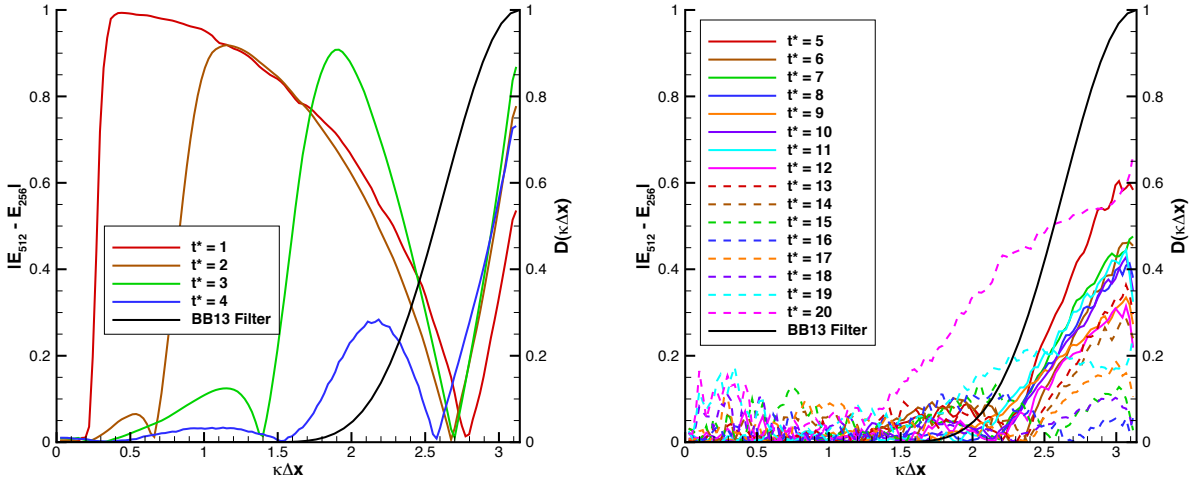

(a) $t^* \leq 4$ (b) $t^* \geq 5$

Figure 12: Error in the energy spectra for the BB13 scheme on the 256^3 grid compared to the damping function of the filter

E. Effect of sub-grid model

All the solutions presented so far have been without any explicit modeling of the sub-grid scale turbulence. Large-eddy simulation sub-grid scale models were examined using the BB13 scheme and the 128^3 grid. Sub-grid models mimic the effect of the small scale turbulence by generating additional dissipation that is intended to affect the resolved turbulent structures. The standard Smagorinsky model and the dynamic Smagorinsky model are compared to the no model case in figure 13. Examining the KEDR curves(figures 13a & 13b), both sub-grid models perform similarly. Early in the simulation the flow contains large coherent structures and a fully turbulent flow has not yet developed. There is no small scale turbulence and the sub-grid model is not needed. However, the sub-grid models do not recognize this and produce dissipation that adds to the overall dissipation in the simulation. This is evidenced by the increased $\epsilon(E_k)$ for $t^* < 8$. Beyond this point, the flow is fully turbulent and the sub-grid model's dissipation acts appropriately, damping the large turbulent structures that are the primary dissipation mechanism. This effect is seen in the reduction of $\epsilon(E_k)$ from the no sub-grid model case for $8 < t^* < 12$. At later times the models perform similarly to the no model case. Because the models add dissipation to the simulation and damp the large scale turbulent structures, they significantly reduce the enstrophy based KEDR (figures 13c & 13d), and increase the disparity between $\epsilon(E_k)$ and $\epsilon(\zeta)$.

The dynamic model produces a jagged $\epsilon(E_k)$ curve at the peak dissipation rates and also produces slightly higher levels of $\epsilon(\zeta)$ at that location. The dynamic model locally varies the Smagorinsky coefficient based on the resolved flowfield. In general, this feature results in a less dissipative sub-grid model and also allows for the backscatter of energy; energy flowing from the sub-grid scales, back to the resolved scales. The jagged appearance of the curve is due to this backscatter effect. This was confirmed with a simulation where backscatter was prevented and the curve became smooth.

The effect of the sub-grid model on the resolved structures can be visualized using vorticity contours (figure 14). The no model case has the highest level of vorticity and a slightly jagged appearance to the contours. The sub-grid model solutions maintain the general characteristics, but the peak vorticity levels are reduced and the contours have been smoothed.

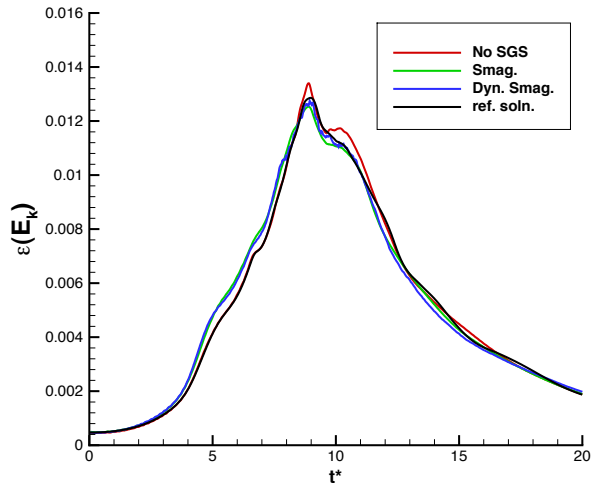

(a) directly computed KEDR, $\epsilon(E_k)$

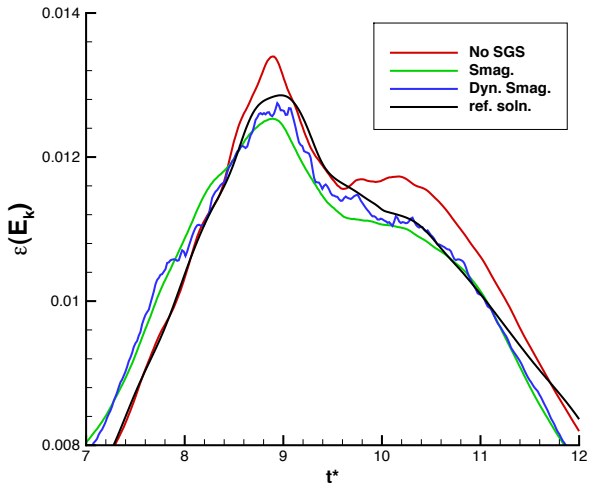

(b) close-up of directly computed KEDR, $\epsilon(E_k)$

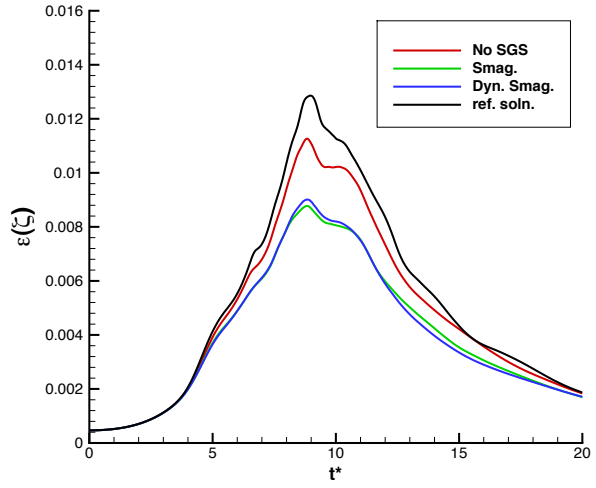

(c) enstrophy based KEDR, $\epsilon(\zeta)$

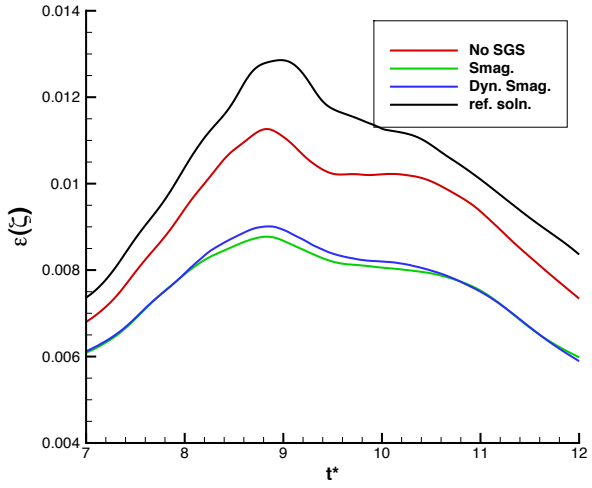

(d) close-up of enstrophy based KEDR, $\epsilon(\zeta)$

Figure 13: Kinetic energy dissipation rate; comparison of sub-grid scale models.

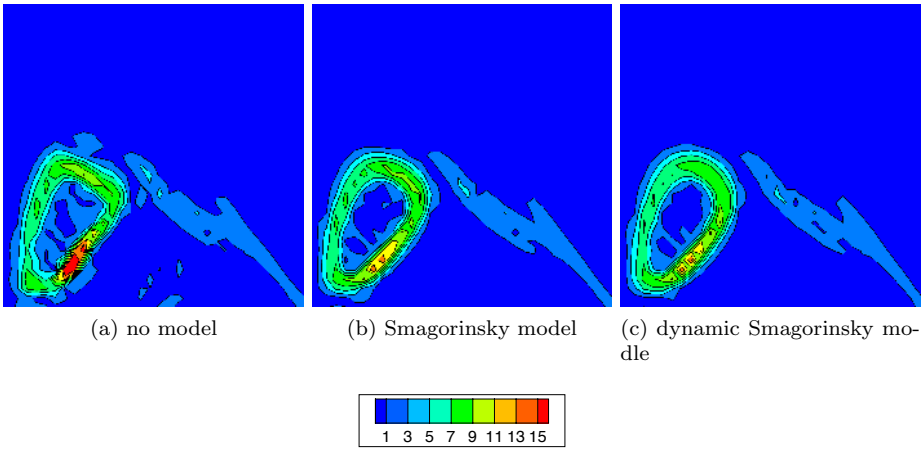

(a) no model (b) Smagorinsky model (c) dynamic Smagorinsky modle

Figure 14: Contours of the vorticity norm $|\omega|\frac{L}{V_0}$, at $t^* = 8$ on the plane $x = -\pi L$, in the region $y = 0$ to $\frac{\pi L}{2}$ and $z = \frac{\pi L}{2}$ to πL; comparison of sub-grid models using the BB13 scheme on the 128^3 grid

F. Effect of high-order viscous terms

It is standard practice in high-order Navier-Stokes codes to limit the high-order schemes to the convective terms and compute the viscous terms with lower order methods. In the case of WRLES and many other codes, fourth-order differencing is used for the viscous derivatives. It has been long assumed that the accuracy of the convective terms is critical for resolving the turbulence and the accuracy of viscous terms is much less important. This treatment reduces computational cost and complexity.

It was suggested at the High-Order CFD workshop that the author investigate the effect of using the same order of accuracy for both convective and viscous derivatives. In this investigation, the standard 12th-order scheme was used for the convective terms and solutions were obtained with both 4th-order and 12th-order accurate viscous terms. Figure 15 shows the results. $\epsilon(E_k)$ is only slightly effected by the high-order viscous terms and no clear trend is visible. However, figure 15b clearly shows that the higher order

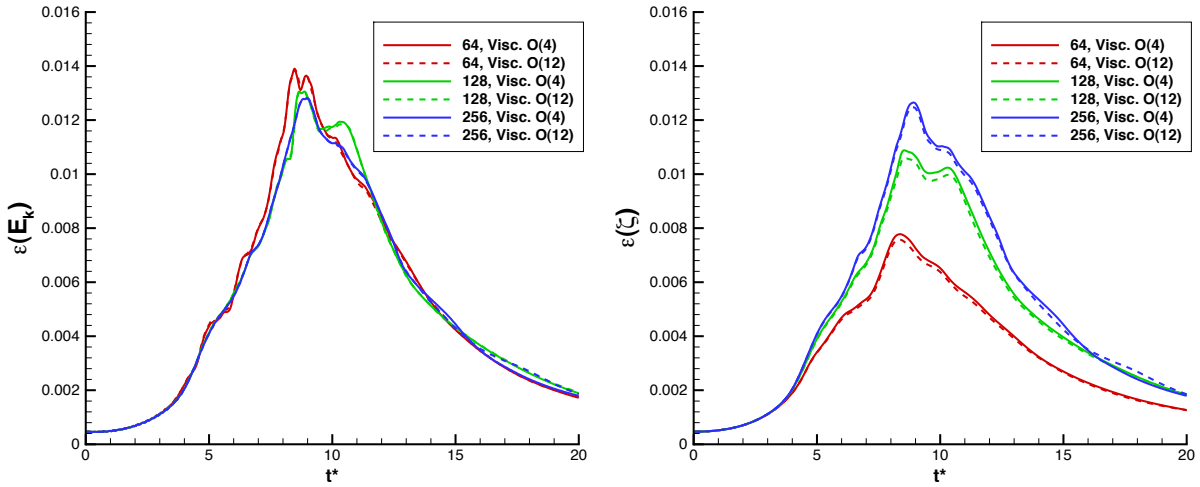

(a) directly computed KEDR, $\epsilon(E_k)$ (b) enstrophy based KEDR, $\epsilon(\zeta)$

Figure 15: Kinetic energy dissipation rate; effect of high-order viscous terms

viscous terms reduce the $\epsilon(\zeta)$. The lower-order representation under-predicts the magnitude of the derivatives used in computing the stress tensor. Using the more accurate higher-order representation results in larger magnitudes for τ_{ij} and hence a more dissipative term in the equations.

V. Conclusions

A numerical study of the Taylor-Green vortex problem was undertaken using central-differencing based finite difference methods. The compressible Navier-Stokes equations were solved using both standard central differencing and Dispersion Relation Preserving differencing schemes. Grids ranging from 64^3 to 512^3 were used.

For the baseline method, Bogey & Bailley's 13-point Dispersion Relation Preserving (DRP) scheme, the kinetic energy dissipation rate (KEDR), computed directly from the kinetic energy in the domain, $\epsilon(E_k)$ was predicted reasonably well at all grid levels, with the largest discrepancies occurring near the peak dissipation rates. A second "theoretical" KEDR based on the enstrophy in the domain, $\epsilon(\zeta)$ was significantly under-predicted on the lower resolution grids. Increasing grid resolution significantly improved the results. Results at the finer grid levels (256^3 and 512^3) were in very good agreement with a reference solution generated with a spectral method.[14]

For many solutions the directly computed KEDR is well predicted and the enstrophy based KEDR is under-predicted. This indicates that: 1) the turbulent structures are under-resolved, 2) the numerical dissipation from the filter plays a significant role in energy dissipation, and 3) the current numerical approach is well suited for implicit large-eddy simulation.

Several spatial differencing schemes were compared: the 13-point DRP scheme of Bogey & Bailley and the 4th, 8th and 12th order central differencing schemes. Results were as expected with the higher-order schemes achieving grid convergence faster than lower-order schemes. To accurately resolve the details of the turbulent structures, high-order schemes are recommended. However, lower-order schemes were shown to adequately resolve the directly computed KEDR. The DRP scheme and 12th order scheme had very comparable solutions; this is expected as they have the same size stencils. The DRP scheme slightly extends the resolved range of the turbulent energy spectra, but this difference is small.

Solution filtering was used to maintain numerical stability and the minimum stable value of the damping coefficient was used for each solution. The filter was shown to behave as designed, damping the poorly resolved high wavenumber structures and leaving low wavenumbers untouched. A pronounced "tailing off" of the energy spectra at the highest wave numbers was shown to be due to the filter. Increasing the filter's damping coefficient increased the KEDR. Increasing damping by using a lower-order filter with a smaller cut-off wavenumber was shown to actually reduce the KEDR because some of the large-scale turbulent structures responsible for the dissipation have been removed.

The effect of large-eddy simulation based sub-grid models were examined at the under-resolved 128^3 grid level. Both the Smagorinsky and dynamic Smagorinsky models were compared. The sub-grid models were found to: 1) add too much dissipation where the flow is not fully turbulent, 2) improve the solution near the peak dissipation rates, 3) dissipate the resolved turbulent structures reducing the peak levels of vorticity, and 4) increase the levels of numerical dissipation. The dynamic model also shows evidence of providing a backscatter of energy into the resolved scales from the sub-grid scales.

Finally, computing the viscous terms with high-order numerics consistent with the convective terms slightly reduces the integrated enstrophy, indicating the numerical dissipation has increased, in comparison with using a fourth-order method.

References

[1]Taylor, G. I. and Green, A. E., "Mechanisms of the Production of Small Eddies from Large Ones," *Proceedings of the Royal Society of London A*, Vol. 158, 1937, pp. 499–521.

[2]DeBonis, J. R., "An Examination of the Spatial Resolution Requirements for LES of a Compressible Jet," *Quality and Reliability of Large-Eddy Simulation II*, edited by M. V. Salvetti, B. Geurts, H. Meyers, and P. Sagaut, Springer, 2010, pp. 329–338.

[3]DeBonis, J. R., "A High-Resolution Capability for Large-Eddy Simulation of Jet Flows," AIAA Paper 2010-5023, 2010.

[4]Forum, M. P. I., *MPI: A Message-Passing Interface Standard, Version 2.2* , High Performance Computing Center Stuttgart (HLRS), 2009.

[5]Chapman, B., Jost, G., and van der Pas, R., *Using OpenMP: Portable Shared Memory Parallel Programming*, The MIT Press, 2007.

[6]Smagorinsky, J., "General Circulation Experiments with the Primitive Equations, Part I: The Basic Experiment," *Monthly Weather Review*, Vol. 91, 1963, pp. 99–152.

[7]Lilly, D. K., "A Proposed Modification of the Germano Subgrid-Scale Closure Method," *Physics of Fluids A*, Vol. 4, No. 3, 1992, pp. 633–635.

[8]Williamson, J. H., "Low-Storage Runge-Kutta Schemes," *Journal of Computational Physics*, Vol. 35, 1980, pp. 48.

[9]Carpenter, M. H. and Kennedy, C. A., "Fourth-Order 2N-Storage Runge-Kutta Schemes," NASA TM 109112, 1994.

[10]Bogey, C. and Bailly, C., "A Family of Low Dispersive and Low Dissipative Explicit Schemes for Flow and Noise Computations," *Journal of Computational Physics*, Vol. 194, 2004, pp. 194–214.

[11]Kennedy, C. A. and Carpenter, M. H., "Comparison of Several Numerical Methods for Simulation of Compressible Shear Layers," NASA TP 3484, 1997.

[12]Vichnevetsky, R. and Bowles, J. B., *Fourier Analysis of Numerical Approximations of Hyperbolic Equations*, Society for Applied and Industrial Mathematics, 1982.

[13]Brachet, M. E., Meiron, D. I., Orszag, S. A., Nickel, B. G., Morf, R. H., and Frisch, U., "Small-scale structure of the Taylor-Green Vortex," *Journal of Fluid Mechanics*, Vol. 130, 1983, pp. 411–452.

[14]van Rees, W. M., Leonard, A., Pullin, D. I., and Koumoutsakos, P., "A Comparison of Vortex and Pseudo-Spectral Methods for the Simulation of Periodic Vortical Flows at High Reynolds Numbers," *Journal of Computational Physics*, Vol. 230, 2011, pp. 2794–2805.

REPORT DOCUMENTATION PAGE	Form Approved OMB No. 0704-0188

1. REPORT DATE *(DD-MM-YYYY)*	2. REPORT TYPE	3. DATES COVERED *(From - To)*
01-02-2013	Technical Memorandum	

4. TITLE AND SUBTITLE
Solutions of the Taylor-Green Vortex Problem Using High-Resolution Explicit Finite Difference Methods

5a. CONTRACT NUMBER

5b. GRANT NUMBER

5c. PROGRAM ELEMENT NUMBER

6. AUTHOR(S)
DeBonis, James, R.

5d. PROJECT NUMBER

5e. TASK NUMBER

5f. WORK UNIT NUMBER
WBS 561581.02.08.03.48.01

7. PERFORMING ORGANIZATION NAME(S) AND ADDRESS(ES)
National Aeronautics and Space Administration
John H. Glenn Research Center at Lewis Field
Cleveland, Ohio 44135-3191

8. PERFORMING ORGANIZATION REPORT NUMBER
E-18637

9. SPONSORING/MONITORING AGENCY NAME(S) AND ADDRESS(ES)
National Aeronautics and Space Administration
Washington, DC 20546-0001

10. SPONSORING/MONITOR'S ACRONYM(S)
NASA

11. SPONSORING/MONITORING REPORT NUMBER
NASA/TM-2013-217850

12. DISTRIBUTION/AVAILABILITY STATEMENT
Unclassified-Unlimited
Subject Categories: 34 and 02
Available electronically at http://www.sti.nasa.gov
This publication is available from the NASA Center for AeroSpace Information, 443-757-5802

13. SUPPLEMENTARY NOTES

14. ABSTRACT
A computational fluid dynamics code that solves the compressible Navier-Stokes equations was applied to the Taylor-Green vortex problem to examine the code's ability to accurately simulate the vortex decay and subsequent turbulence. The code, WRLES (Wave Resolving Large-Eddy Simulation), uses explicit central-differencing to compute the spatial derivatives and explicit Low Dispersion Runge-Kutta methods for the temporal discretization. The flow was first studied and characterized using Bogey & Bailley's 13-point dispersion relation preserving (DRP) scheme. The kinetic energy dissipation rate, computed both directly and from the enstrophy field, vorticity contours, and the energy spectra are examined. Results are in excellent agreement with a reference solution obtained using a spectral method and provide insight into computations of turbulent flows. In addition the following studies were performed: a comparison of 4th-, 8th-, 12th- and DRP spatial differencing schemes, the effect of the solution filtering on the results, the effect of large-eddy simulation sub-grid scale models, and the effect of high-order discretization of the viscous terms.

15. SUBJECT TERMS
Turbulence; Computational fluid dynamics; Vorticity; Large-eddy simulation; Direct numerical simulation

16. SECURITY CLASSIFICATION OF:			17. LIMITATION OF ABSTRACT	18. NUMBER OF PAGES	19a. NAME OF RESPONSIBLE PERSON
a. REPORT	b. ABSTRACT	c. THIS PAGE			STI Help Desk (email:help@sti.nasa.gov)
U	U	U	UU	28	19b. TELEPHONE NUMBER *(include area code)* 443-757-5802